Enhanced Survival with Implantable Scaffolds That Capture Metastatic Breast Cancer Cells *In Vivo*

Shreyas S. Rao[1], Grace G. Bushnell[2], Samira M. Azarin[3], Graham Spicer[4], Brian A. Aguado[5], Jenna R. Stoehr[6], Eric J. Jiang[4], Vadim Backman[7], Lonnie D. Shea[2,8], and Jacqueline S. Jeruss[2,9]

Abstract

The onset of distant organ metastasis from primary breast cancer marks the transition to a stage IV diagnosis. Standard imaging modalities often detect distant metastasis when the burden of disease is high, underscoring the need for improved methods of detection to allow for interventions that would impede disease progression. Here, microporous poly(ε-caprolactone) scaffolds were developed that capture early metastatic cells and thus serve as a sentinel for early detection. These scaffolds were used to characterize the dynamic immune response to the implant spanning the acute and chronic foreign body response. The immune cell composition had stabilized at the scaffold after approximately 1 month and changed dramatically within days to weeks after tumor inoculation, with $CD11b^+Gr1^{hi}Ly6C^-$ cells having the greatest increase in abundance. Implanted scaffolds recruited metastatic cancer cells that were inoculated into the mammary fat pad *in vivo*, which also significantly reduced tumor burden in the liver and brain. Additionally, cancer cells could be detected using a label-free imaging modality termed inverse spectroscopic optical coherence tomography, and we tested the hypothesis that subsequent removal of the primary tumor after early detection would enhance survival. Surgical removal of the primary tumor following cancer cell detection in the scaffold significantly improved disease-specific survival. The enhanced disease-specific survival was associated with a systemic reduction in the $CD11b^+Gr1^{hi}Ly6C^-$ cells as a consequence of the implant, which was further supported by Gr-1 depletion studies. Implementation of the scaffold may provide diagnostic and therapeutic options for cancer patients in both the high-risk and adjuvant treatment settings. *Cancer Res; 76(18); 5209–18. ©2016 AACR.*

Introduction

The oncogenic progression of breast cancer from the primary tumor to distant metastatic sites is the critical event that defines stage IV disease (1–3). Currently, metastatic disease is detected through radiologic imaging modalities after the burden of distant disease has become destructive to the host organ (4–6). A limitation to the development of life-preserving timely interventions is the striking lack of robust technologies capable of early detection of metastatic events. Additionally, experimental model systems are needed that permit systematic screening and examination of factors contributing to breast cancer metastasis in a controlled setting. Detection of circulating tumor cells (CTC) is being pursued in both the experimental and clinical settings. While promising (7, 8), the widespread use of CTC capture is not without challenges, given the high biomarker sensitivity and specificity required to capture a low number of circulating CTCs (9, 10). Furthermore, CTCs may not represent the population of cells capable of metastasis or these cells could circulate for long periods before invading distant organs. The capacity to identify metastatic cells or foci at the earliest possible time point may permit the delivery of targeted treatment interventions prior to the compromise of distant organs, potentially translating into prolonged distant metastasis-free outcomes. Thus, there is an urgent need for development of novel technologies to aid in the detection of metastatic events in the nascent setting.

An emerging approach for early detection lies with the implantation of a biomaterial scaffold that can capture metastatic cells (11). These scaffolds were modeled after the concept of the premetastatic niche (12, 13), echoing Paget's "seed and soil" hypothesis proposed over a century ago (12, 14–17). This paradigm

[1]Department of Chemical and Biological Engineering, University of Alabama, Tuscaloosa, Alabama. [2]Department of Biomedical Engineering, University of Michigan, Ann Arbor, Michigan. [3]Department of Chemical Engineering and Materials Science, University of Minnesota, Minneapolis, Minnesota. [4]Department of Chemical and Biological Engineering, Northwestern University, Evanston, Illinois. [5]Department of Chemical and Biological Engineering, University of Colorado, Boulder, Colorado. [6]Weinberg College of Arts and Sciences, Northwestern University, Evanston, Illinois. [7]Department of Biomedical Engineering, Northwestern University, Evanston, Illinois. [8]Department of Chemical Engineering, University of Michigan, Ann Arbor, Michigan. [9]Department of Surgery, University of Michigan, Ann Arbor, Michigan.

Corresponding Authors: Lonnie D. Shea, Department of Biomedical Engineering, The University of Michigan, 1119 Carl A. Gerstacker Building, 2200 Bonisteel Boulevard, Ann Arbor, MI 48109. Phone: 734-764-7149; Fax: 734-936-1905; E-mail: ldshea@umich.edu; and Jacqueline S. Jeruss, Departments of Surgery, Pathology, and Biomedical Engineering, Division of Surgical Oncology, University of Michigan, 3303 Cancer Center, 1500 East Medical Center Drive, Ann Arbor, MI 48109-5932. Phone: 734-615-4823; Fax: 734-647-9647; E-mail: jjeruss@med.umich.edu

proposes that, prior to colonization by metastatic cells, supportive cells (e.g., fibroblasts, immune cells, and endothelial cells), soluble factors, and extracellular matrix (ECM) components establish a microenvironment conducive to tumor cell homing and colonization (12, 14–17). Importantly, these studies indicate that metastasis to specific organs is not random, but is influenced by the properties of the local environment (12, 13, 18). The initial translation of these principles led to the development and implementation of microporous poly(lactide-co-glycolide) (PLG) biomaterial scaffolds, which recruited metastatic breast cancer cells through the local immune response *in vivo*, resulting in decreased tumor burden at metastatic sites (11). However, PLG scaffolds were degradable over time scales considered too short for clinical translation.

In this report, we developed microporous poly(ε-caprolactone) (PCL) scaffolds with greater stability than the PLG scaffolds, to investigate the dynamic immune response and cellular events associated with PCL scaffold–mediated recruitment of metastatic breast cancer cells. Specifically, utilizing PCL scaffolds in metastatic breast cancer murine models we examined if (i) metastatic cells could be recruited to the scaffold; (ii) metastatic cells could be detected in the scaffold at a nascent stage, prior to cancer cell colonization of other major organs, using label-free imaging modalities; and (iii) scaffold implantation could influence survival following detection of cancer cells in the scaffold and then subsequent surgical removal of the primary tumor. The favorable translational endpoints from these studies could lead to the integration of scaffold implants, fabricated using FDA-approved materials, into breast cancer disease management plans. Moreover, scaffolds could be recovered to examine the biology of metastatic tumor cells in conjunction with "niche" cells enabling the development of patient-specific treatments.

Materials and Methods

Fabrication, characterization, and implantation of microporous scaffolds

Scaffold fabrication and characterization. For the preparation of microporous PCL scaffolds, PCL microspheres were first prepared by emulsifying a 6% (w/w) solution of PCL (Lactel Absorbable Polymers; Inherent viscosity = 0.65–0.85 dL/g) in dichloromethane in a 10 % poly(vinyl alcohol) solution followed by homogenization at 10,000 rpm for ∼1 minute. The solution was then stirred for 3 hours. Microspheres were collected by centrifugation and washed at least 5 times in deionized water, followed by lyophilization for 48 hours. To prepare microporous PCL scaffolds, PCL microspheres and salt particles (size range, 250–425 μm) were mixed in a 1:30 (w/w) ratio and pressed at 1,500 psi in a steel die for ∼45 seconds. Polymer-salt discs were heated at 60°C for ∼5 minutes on each side, followed by foaming in high pressure CO_2 at 800 psi for ∼24 hours. Salt particles were removed by immersing discs in water. For experimental studies, scaffolds were sterilized using 70% ethanol, rinsed with sterile water, and dried on a sterile gauze pad. Microporous PLG scaffolds were prepared as described previously (19). Scaffolds were characterized using mechanical testing, scanning electron microscopy, and calculation of porosity. Technical details are available in Supplementary Materials and Methods.

Scaffold implantation. Microporous scaffolds were implanted in the subcutaneous space of either female BALB/c or NOD/SCID-IL2Rγ$^{-/-}$ (NSG) mice (8–10-week-old). All animal studies were performed in accordance with institutional guidelines and protocols approved by Northwestern University and the University of Michigan Institutional Animal Care and Use Committee. NSG mice were bred in house or purchased from the Jackson laboratory. BALB/c mice were purchased from The Jackson laboratory. For the implantation procedure, mice were anesthetized with an intraperitoneal injection of Ketamine (100 mg/kg) and Xylazine (5 mg/kg). The upper back was shaved and prepped using a betadine swab followed by an ethanol swab (3X). An incision was made in the upper back, and a subcutaneous pocket was created on each side, into which the scaffolds were inserted (2 scaffolds per mouse). The skin was closed using wound clips (Reflex 7 mm, Roboz Surgical Instrument Co.) and surgical glue (3M Vetbond Tissue Adhesive).

Tumor inoculation

Orthotopic tumor inoculation was performed 1 month after scaffold implantation. MDA-MB-231BR-tdTomato-luc2 cells were obtained from the Northwestern University Developmental Therapeutics Core and authenticated by short tandem repeat DNA analysis and comparison to the ATCC STR profile database in 2013 (DDC Medical). 4T1-luc2-tdTomato cells were obtained from Perkin Elmer in 2014 and were used directly without additional authentication. A total of 2×10^6 4T1-luc2-tdTomato (Perkin Elmer) or MDA-MB-231BR-tdTomato-luc2 cells in 50 μL sterile phosphate buffer saline (PBS; Life Technologies) were injected into the fourth right mammary fat pad of 12- to 14-week-old female BALB/c or NSG mice.

Flow cytometry

Mice were euthanized at indicated times, and retrieved scaffolds and organs were processed according to previously established procedures, which are described in Supplementary Materials and Methods (11). Flow cytometry staining and analysis were performed according to established procedures (please see Supplementary Materials and Methods; ref. 11).

Scaffold sectioning and fluorescence imaging

Scaffolds retrieved from mice were rinsed in PBS and then immediately flash frozen in pre-chilled isopentane. Frozen scaffolds were then embedded in optimal cutting temperature (Cardinal Health) compound with 30% sucrose and sectioned using a cryostat (Microm HM 525; Microm International) at 14 μm. Scaffold sections were stored at −20°C until imaging. Cryosections were air-dried at room temperature for 30 minutes, fixed with 10% neutral-buffered formalin, washed with tap water for 5 minutes, DI water for 10 minutes (2X) and cover slipped with ProLong Gold antifade aqueous mounting medium containing DAPI (Molecular Probes). DAPI fluorescence was visualized using an excitation wavelength of 358 nm, and tdTomato fluorescence in cancer cells was visualized using an excitation wavelength of 532 nm. Images were viewed using an Olympus BX43 microscope, and an Olympus DP72 digital camera with CellSens Entry software (Olympus) was used for image capture and colocalization.

Inverse spectroscopic optical coherence tomography imaging and analysis

Inverse spectroscopic optical coherence tomography (ISOCT) imaging and analysis was performed as described elsewhere

(20–22). Technical details about this procedure are provided in Supplementary Materials and Methods.

Post-surgical model of breast cancer metastasis and Gr-1 depletion

The influence of scaffold implant on survival was investigated using a post-surgical model of breast cancer metastasis (23, 24). In this model, the 4T1 primary tumor was resected 6 or 10 days after tumor inoculation. Briefly, the primary tumor area was prepped using a betadine swab followed by an ethanol swab (3X). An incision was made along the right side of the lower half of the dorsal skin exposing the primary tumor. The tumor was picked up using needle nose-forceps and cut around the base using curved tip scissors. The skin was closed using MONOCRYL (poligleca-prone 25) suture (Ethicon, Inc.) and surgical glue (3M Vetbond Tissue Adhesive). Animal health was monitored daily after the procedure for activity and responsiveness, including posture, mobility, body weight, grooming behavior, and respiratory conditions. Animals were euthanized if found in a moribund condition as an experimental endpoint. Mice that evidenced primary tumor re-growth were excluded from the analysis to avoid confounding effects arising from the primary tumor. For Gr-1 depletion studies, resection was performed at day 10 as described above and mice received 300 µg anti-Gr-1 (clone RB6-8C5, Bio X Cell) via intraperitoneal injection at days 13 and 17 after tumor inoculation.

Data analysis

Data are presented as mean $\pm$ standard error (SEM). Animal studies were performed with at least two independent replicates of 4 to 8 female 8–12-week-old mice per group with random assignment. Multiple comparisons were performed using one-way ANOVA. Comparisons post ANOVA was performed using the Tukey HSD test. For data that did not follow a normal distribution, comparison was performed using the nonparametric Wilcoxon rank-sum test. For comparing the relative number of mice containing detectable tumor cells in organs with scaffolds, a Fisher exact test was used to determine the P value. Statistical analysis was performed using JMP Software (JMP Pro 11). For survival analysis, the Kaplan–Meier curve was generated, and statistical analysis was performed using a Log-rank test using Sigma Plot (Version 13).

Results

### Microporous PCL scaffolds for *in vivo* recruitment of metastatic cells

We developed microporous PCL scaffolds (Fig. 1A, 5 mm diameter and 2 mm height) to create microenvironments *in vivo* and subsequently examine their ability to recruit metastatic tumor cells. The porous interconnected architecture of the scaffold was confirmed using SEM imaging (Fig. 1B). Microstructural features, such as porosity, pore volume, and mechanical properties (i.e., elastic modulus), were similar for PCL and previously reported PLG scaffolds (Supplementary Table S1; ref. 11). The ability of PCL scaffolds to persist and create a defined space *in vivo* was investigated by implantation into the subcutaneous dorsal space of BALB/c and NSG mice. The subcutaneous site was selected for its accessibility and amenability to noninvasive imaging. Furthermore, neither 4T1 nor MDA-MB-231BR breast cancer cells typically metastasize to the subcutaneous space, thus the presence of cancer cells in the metastatic site would likely be associated with

the presence of the scaffold. PCL scaffolds retrieved after 3 months experienced minimal degradation when compared with day 0 as opposed to PLG scaffolds, which had previously been used for *in vivo* recruitment of tumor cells (11). PLG scaffolds showed significant degradation over this time period as quantified by scaffold area (i.e., 66% in NSG and 77% in BALB/c mouse; Supplementary Fig. S1).

The dynamic immune response to the biomaterial implant was investigated throughout the acute and chronic phases. Implantation of the PCL scaffold into healthy BALB/c mice resulted in infiltration of CD45$^+$ leukocytes by day 3. The number of CD45$^+$ leukocytes remained relatively unchanged after day 14 post scaffold implantation (Fig. 1C). However, the relative distribution of leukocyte populations examined, including innate and adaptive immune cells, changed dynamically following scaffold implantation. The percentage of inflammatory monocytes, identified as Ly6C$^+$F4/80$^-$ cells, decreased after day 3 and remained relatively stable at later time points, whereas the percentage of dendritic cells, identified as CD11c$^+$F4/80$^-$, increased after day 3 and remained stable at later time points (Fig. 1D). These two cell populations constituted the majority of cells (i.e., $\geq$65%) observed at the PCL scaffold at later time points. The percentage of macrophages, identified as CD11b$^+$F4/80$^+$ cells, significantly increased through day 14 (e.g., 8.8% at day 14 vs. 1.7% at day 3, Fig. 1D, $P < 0.05$) and then returned to levels observed at day 3 (e.g., 1.4 % at day 60, Fig. 1D, $P = 0.99$ compared with day 3). In contrast, the levels of CD11b$^+$Gr-1^{hi}Ly6C$^-$ cells remained low at all time points examined at 0.15 % (Fig. 1D). In the adaptive immune cell population, the percentage of CD4$^+$ helper T cells and CD8$^+$ cytotoxic T cells significantly increased over time (e.g., 1% at day 3 to 9% at day 60 for CD4$^+$ and 1.2% at day 3 to 3% at day 60 for CD8$^+$, respectively, Fig. 1D, $P < 0.05$). The percentage of B cells, identified as CD19$^+$, and natural killer (NK) cells, identified as CD49b$^+$, increased post day 3 and returned to day 3 levels at later time points (i.e., days 30 and 60; Fig. 1D). Importantly, the relative percentages of leukocyte subpopulations were similar between day 30 and day 60 after scaffold implantation in BALB/c mice (Fig. 1D). This trend was also observed in NSG mice (Supplementary Fig. S2). Based on the stabilization of cell populations after day 30, we utilized day 30 as a time point representing the chronic response to a scaffold implant in all following experiments.

We subsequently examined the recruitment of metastatic cells to a chronically implanted microporous scaffold (i.e., a scaffold that had been implanted for 30 days prior to tumor inoculation, a time corresponding to the chronic phase of the immune response). Flow cytometry and fluorescence imaging (Fig. 2) performed for scaffolds retrieved at day 15 after tumor inoculation demonstrated the presence of mouse 4T1 tumor cells in the scaffold, indicating that the local microenvironment enabled recruitment of tumor cells. Total cell infiltration was significantly greater within PCL scaffolds compared with PLG scaffolds (i.e., $\sim$6 × 10^5 cells in the PCL scaffold vs. $\sim$1 × 10^5 cells in the PLG scaffold, $P < 0.0001$, Fig. 2A) and a similar trend was observed for tumor cell recruitment (Fig. 2B, $P < 0.01$). Scaffolds were also able to recruit human MDA-MB-231BR cells in NSG mice (Supplementary Fig. S4), indicating that such a system enabled recruitment of mouse and human breast cancer cells in the context of both immune competent and immune compromised mouse models, respectively.

Following tumor inoculation, the dynamics of immune cell populations at the PCL scaffold was subsequently
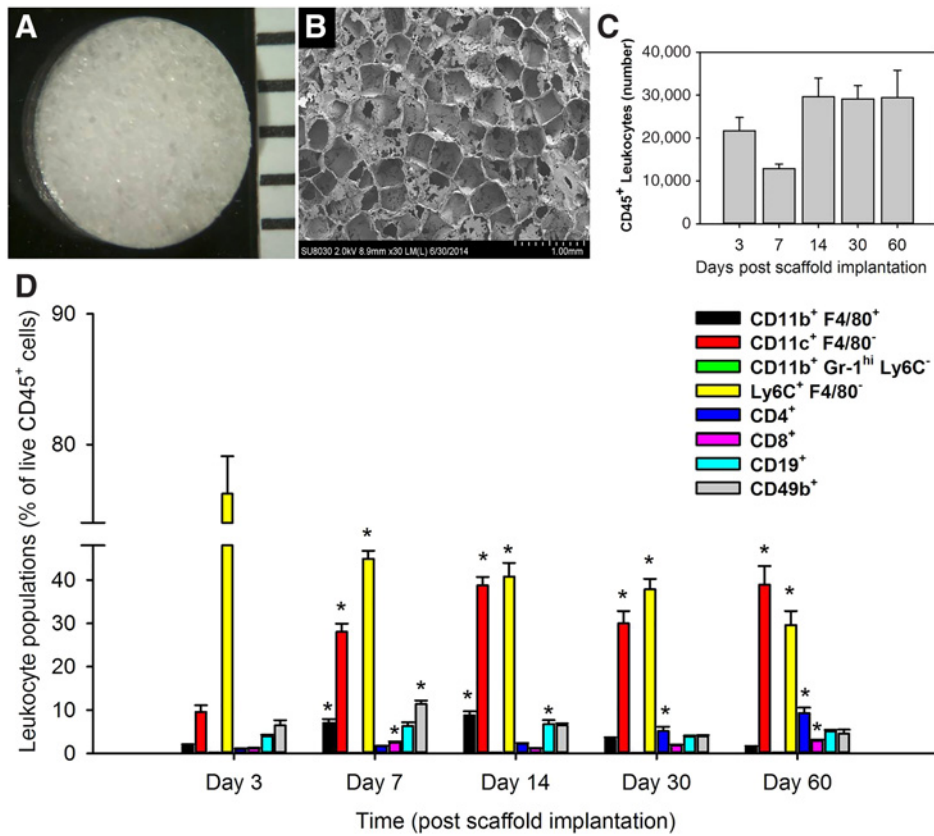
Figure 1.
Physical characteristics and dynamic immune cell response following implantation of microporous PCL scaffolds into the dorsal subcutaneous space of a BALB/c mouse. Photomicrograph (**A**) and scanning electron micrograph (**B**) of a microporous PCL scaffold. SEM image shows the interconnected porous structure. **C** and **D,** CD45$^+$ leukocyte numbers (**C**) and dynamics of CD11b$^+$F4/80$^+$, CD11c$^+$F4/80$^-$, CD11b$^+$Gr-1^{hi}Ly6C$^-$, Ly6C$^+$F4/80$^-$, CD4$^+$, CD8$^+$, CD19$^+$, and CD49b$^+$ immune cell populations expressed as a percentage of live CD45$^+$ leukocytes at days 3, 7, 14, 30, and 60 after PCL scaffold implantation (**D**; $N \geq 6$ for each time point examined; *, $P < 0.05$ compared with day 3 as determined by the Tukey HSD test post ANOVA). Error bars, SEM.

characterized, as tumor cells are known to influence the recruitment of immune cells from the bone marrow (25). Flow cytometric analysis indicated an increase in Ly6C$^+$F4/80$^-$ and CD11b$^+$Gr-1^{hi}Ly6C$^-$ cells at the PCL scaffold site (Fig. 3C and D, $P < 0.0005$). For example, the numbers of CD11b$^+$Gr-1^{hi}Ly6C$^-$ cells increased from 0.1 % at day 0 to 17 % at day 21 after tumor inoculation ($P < 0.05$), an increase of 2 orders of magnitude relative to their numbers at the PCL scaffold site in tumor-free BALB/c mice (Figs. 1D and 3C). Both cell types have been implicated in the pre-metastatic niche (15, 25–28). In contrast, the percentages of CD11b$^+$F4/80$^+$ macrophages, CD11c$^+$F4/80$^-$ dendritic cells, and CD8$^+$ cytotoxic T cells decreased at the PCL scaffold site (Fig. 3A, C and F, e.g., 30% at day 0 vs. 14% at day 21 for dendritic cells, $P < 0.05$). The percentage of CD19$^+$ B cells, CD49b$^+$ NK cells, and CD4$^+$ helper T cells increased at day 3 and then decreased at later time points (Fig. 3G, H and E). Specifically, NK cells increased from 4% at day 0 to 8% at day 3, followed by a decrease to 2.5% at day 21 after tumor inoculation (Fig. 3H, $P < 0.05$). Interestingly, the immune cell dynamics at the PCL scaffold site reflected the dynamics observed in the spleen after tumor inoculation (Fig. 3 vs. Supplementary Fig. S3). In summary, the changing immune microenvironment at the PCL scaffold site after tumor inoculation correlated with recruitment of 4T1 tumor cells, and is consistent with prior literature reports on the role of the immune cells in the pre-metastatic niche (15, 25–30).

### Early detection of metastatic cells at the PCL scaffold

The ability to detect the presence of metastatic disease at an early stage was examined through evaluation of the percentage of tumor cells in the PCL scaffold relative to the cancer cells detected in typical metastatic sites such as the lung, liver, and brain, at day 5 after tumor inoculation. Flow cytometry analysis revealed that the PCL scaffolds had a detectable percentage of tumor cells (i.e., 0.005% ± 0.002%) compared with the lung, liver, and the brain, none of which had detectable tumor cells (Fig. 4A and B; $N = 5$ for lung, liver, and brain, $N = 10$ for PCL scaffolds, $P < 0.05$, Fisher exact test). The greater density of tumor cells observed at the PCL scaffold site compared with other organ sites supports the use of this tool for detecting metastatic disease at a nascent stage.

We subsequently investigated the feasibility of using a label-free imaging technique, ISOCT, for the early detection of metastatic disease in a chronic model of scaffold implantation. The tissue was modeled as a continuous random refractive index distribution, which enabled the refractive index correlation function shape factor D to be computed from the shape of the backscattering intensity spectrum obtained with ISOCT (20). If D has a value between 0 and 3, it has a physical meaning of a mass fractal dimension, reflecting a more clumped structure associated with higher D. Prior studies of early carcinogenesis with ISOCT and a similar spectroscopic technique, low-coherence enhanced backscattering spectroscopy, have revealed that D measured from tissue increases with cancer progression (22, 31, 32). Thus, similar ultra-structural tissue modifications occurring in the pre-metastatic niche are likely to have an analogous effect on D. D has previously been reported to reflect mass–density distribution features at length scales of 35 to 350 nm (21). In addition, D values from tissue have been demonstrated as a robust biomarker of early-stage carcinogenesis (22). Consistent with these
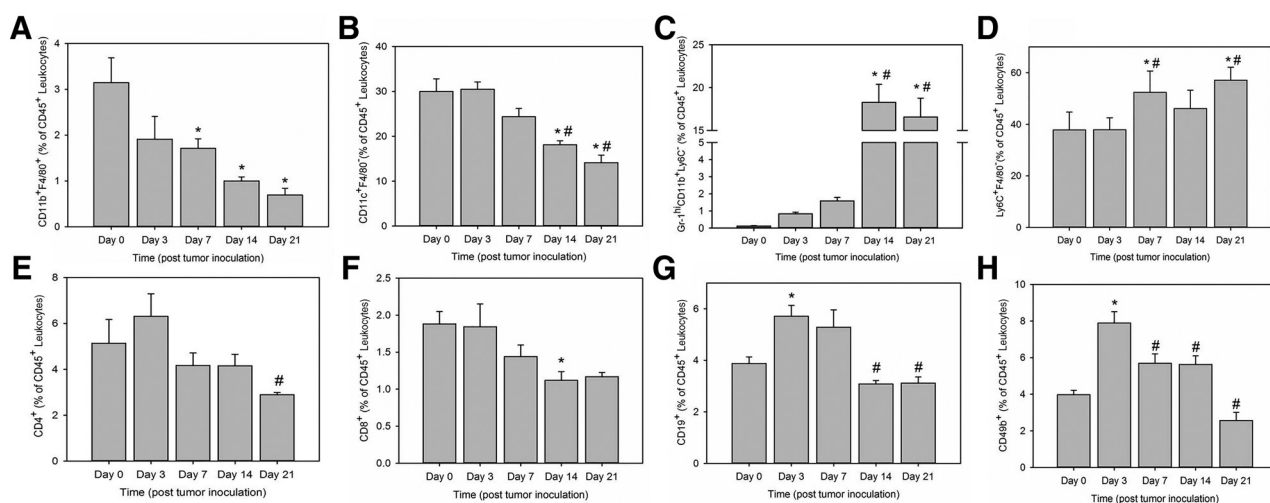
Figure 2.
Microporous scaffolds implanted for 30 days prior to tumor inoculation recruit metastatic cells. Number of total cells (**A**) and tumor cells (tdTomato+ cells; **B**) isolated from microporous PLG and PCL scaffolds at day 15 after tumor inoculation analyzed via flow cytometry ($N = 10$; *, $P < 0.01$ as determined by the t test for analysis of total cell numbers and the Wilcoxon rank-sum test for tumor cell numbers). Fluorescence image of a PCL scaffold section shows the presence of a tumor cell (indicated by white arrow) as identified using tdTomato (**C**) and DAPI (**D**) fluorescence and their colocalization (**E**). Scale bar, 20 μm. Error bars, SEM.
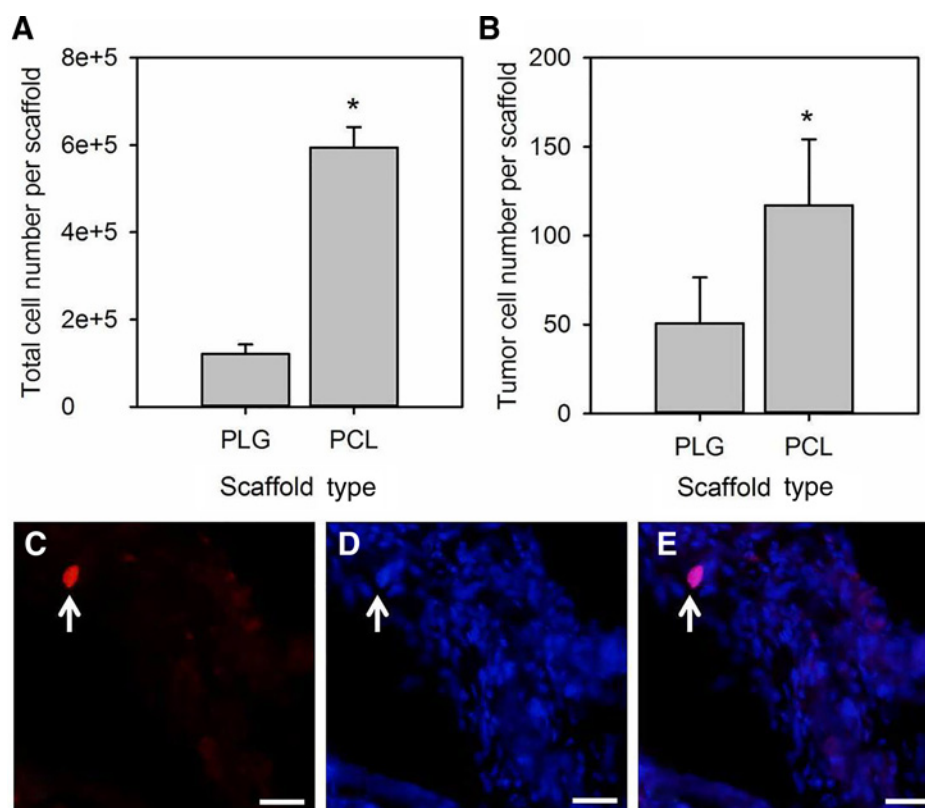
observations and data obtained via flow cytometric analysis (Fig. 4A and B), a significant increase was observed in average D values obtained from ISOCT measurements at the PCL scaffold site in tumor-bearing mice ($N = 7$) compared with tumor-free mice ($N = 8$; $P < 0.05$, Fig. 4C), confirming ultra-structural

alterations to the scaffold and further indicative of the presence of tumor cells. The color map overlay of D values (Fig. 4D and E) demonstrated the distribution throughout the scaffold. These results suggest that ISOCT could be used for early detection of metastatic disease at the PCL scaffold.

Figure 3.
Tumor progression influences dynamics of leukocyte populations at the PCL scaffold. Percentage of CD11b+F4/80+ (**A**), CD11c+F4/80− (**B**), Gr-1hiCD11b+Ly6C− (**C**), Ly6C+F4/80− (**D**) innate immune cell populations and percentage of CD4+ (**E**), CD8+ (**F**), CD19+ (**G**), and CD49b+ (**H**) adaptive immune cell populations in the total population of live CD45+ leukocytes at days 0, 3, 7, 14, and 21 after tumor inoculation ($N \geq 8$ for each time point examined; *, $P < 0.05$ compared with day 0; #, $P < 0.05$ compared with day 3 as determined by the Tukey HSD test post ANOVA). Error bars, SEM.
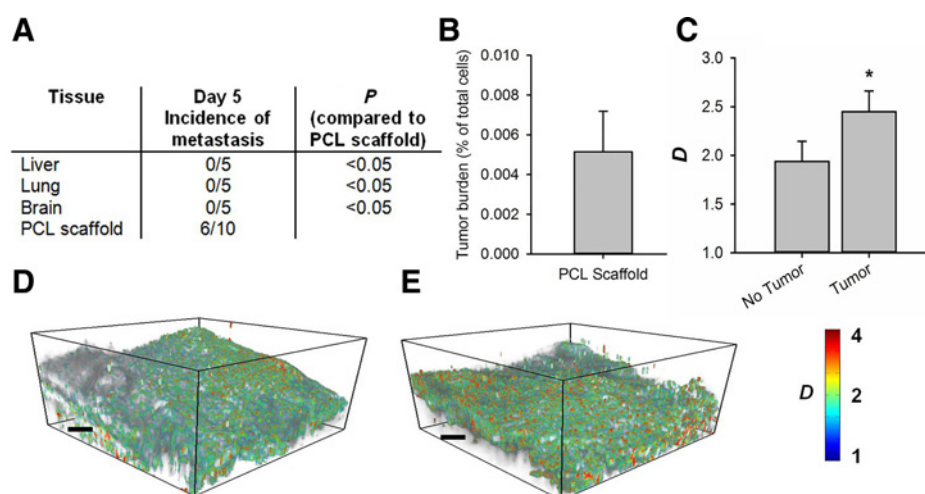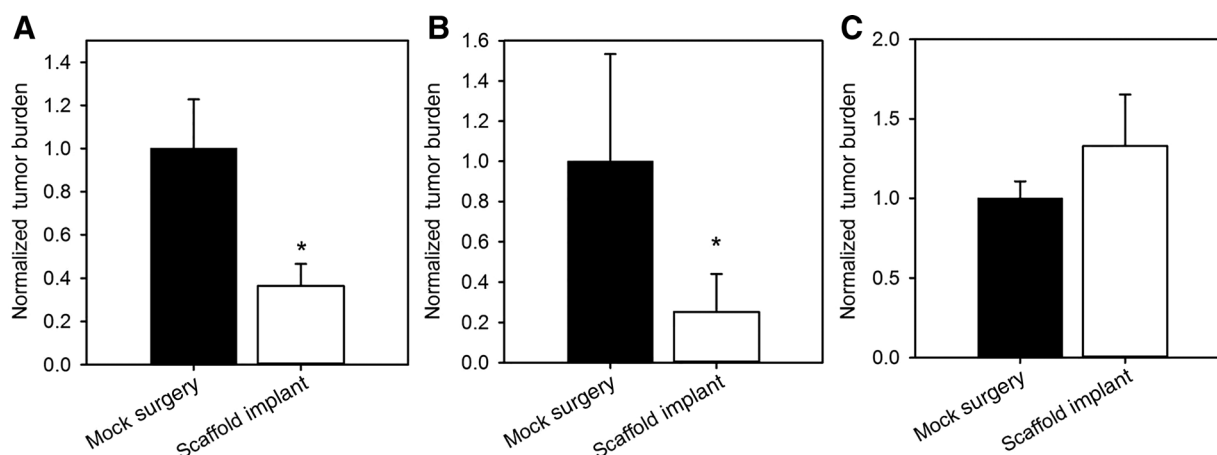
Figure 4.
Microporous PCL scaffolds enable early detection of metastatic cells in a chronic model of scaffold implantation. **A,** number of mice with detectable tumor cells analyzed by flow cytometry in the lung, liver, and brain in a group of 5 mice at day 5 after tumor inoculation ($N = 5$ for lung, brain, and liver; $N = 10$ for PCL scaffolds; *, $P < 0.05$, as determined using the Fisher exact test). **B,** percentage of tdTomato+ tumor cells isolated from the PCL scaffold at day 5 after tumor inoculation analyzed via flow cytometry. **C,** average D value for PCL scaffolds isolated from tumor-free and tumor-bearing mice. Scaffolds from tumor-bearing mice were isolated at day 5 after tumor inoculation ($N = 14$ scaffolds for tumor-free and $N = 16$ scaffolds for tumor-bearing mice; *, $P < 0.05$, as determined using the Wilcoxon rank-sum test). Representative three-dimensional maps of D generated via ISOCT analysis of PCL scaffolds in tumor-free (**D**) and tumor-bearing mice (**E**). Scale bars, 200 μm. Error bars, SEM.

PCL scaffold implantation reduces tumor burden and improves disease-specific survival

We subsequently investigated the hypothesis that the recruitment of metastatic cells to the chronically implanted PCL scaffolds may reduce the tumor burden at typical metastatic sites, such as the liver, brain, and the lung at day 15 after tumor inoculation. Flow cytometry analysis indicated that the percentage of tumor cells in the liver and the brain was reduced in mice receiving a PCL scaffold versus mice undergoing a mock surgery. As stated, the tumor burden was reduced by 64% for the liver (Fig. 5A, $N = 15$, $P < 0.05$) and 75% for the brain (Fig. 5B, $N = 8$ for mock surgery,

$N = 6$ for scaffold implant, $P < 0.05$ as determined using the Wilcoxon rank-sum test in both cases). However, in this immunocompetent mouse model, a reduction in the tumor burden in the lung was not observed (Fig. 5C, $N = 11$, $P = 0.7$) distinct from our previous observations in an immune compromised NSG mouse inoculated with human MDA-MB-231BR cells (11).

A post-surgical model of breast cancer metastasis was then applied to investigate the potential for PCL scaffold implants to influence survival. In this model, the primary tumor was resected at day 6 (Supplementary Fig. S5) or 10 (Fig. 6A) after tumor inoculation, which corresponded to a time after which cancer cells

Figure 5.
Recruitment of 4T1 tumor cells to the PCL scaffold site reduces tumor burden in metastatic sites such as the liver and brain in a chronic model of scaffold implantation in BALB/c mice. Normalized average tumor burden in the liver (**A**), brain (**B**), and the lung (**C**) for the scaffold and mock surgery groups. The average burden in the mock group was set to 1 ($N \geq 6$ for each group; *, $P < 0.05$ compared with mock surgery as determined by the Wilcoxon rank-sum test). Tumor burden in the lung was identical in both groups. Error bars, SEM.

Figure 6.
Microporous PCL scaffolds improve survival in a post-surgical model of breast cancer metastasis. **A,** schematic of experimental design to examine the influence of scaffold implant on survival. **B,** average resected tumor weights for mock and scaffold group were identical ($P = 0.93$, t test). **C,** Kaplan–Meier survival curve for mice undergoing mock surgery versus mice receiving a scaffold implant ($N = 7$ for each group; *, $P < 0.05$ as determined using the log-rank test). Error bars, SEM.
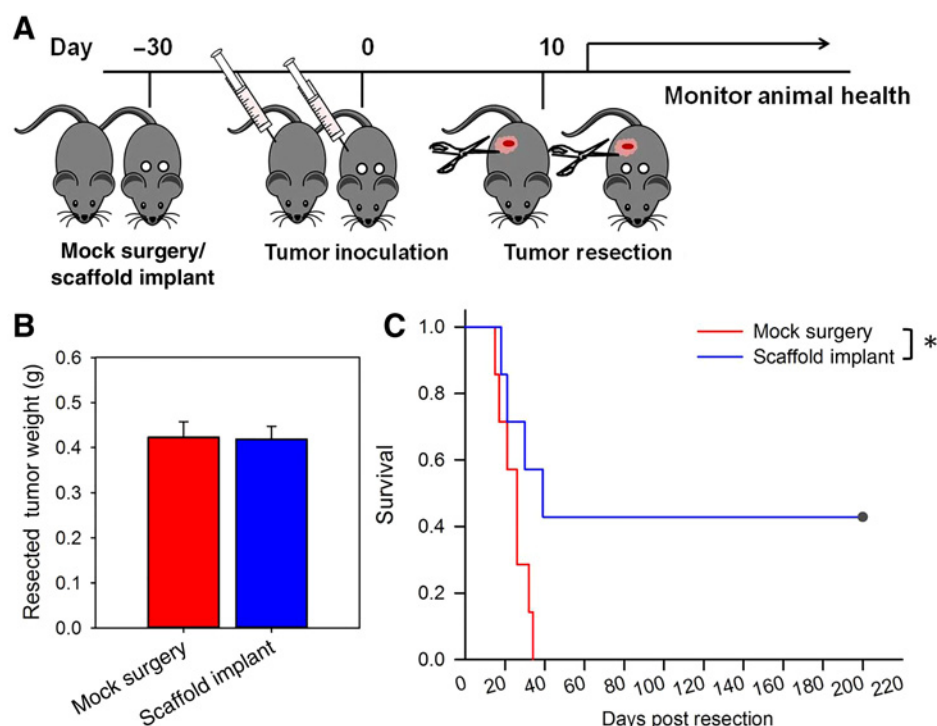
were detectable in the scaffold by label-free imaging (i.e., day 5, Fig. 4). The resected tumor weights were comparable for both groups, with tumors from the mock surgery group weighing 0.423 ± 0.035 g versus tumors from scaffold implanted mice weighing 0.419 ± 0.029 g at day 10 after inoculation ($P = 0.93$, t-test, Fig. 6B). Kaplan–Meier survival analysis demonstrated a significant improvement in survival in mice receiving a PCL scaffold implant compared to mice receiving a mock surgery with resection at day 10 (Fig. 6C, $N = 7$ per group, $P < 0.05$, log-rank test). The sacrifice endpoints utilized for mice in both groups for data corresponding to Fig. 6 are described in Supplementary Table S2. With resection at day 6 after tumor inoculation, ~40% of both mock and scaffold groups survived indefinitely (Supplementary Fig. S5), mirroring the 40% survival in the scaffold group with day 10 resection (Fig. 6C), indicating that the scaffold increased the time over which a therapeutic intervention such as surgery can be performed and provide a survival benefit.

Given the greatest increase in the abundance of CD11b⁺Gr-1^{hi}Ly6C⁻ cells (2 orders of magnitude change) at the PCL scaffold site after tumor inoculation, we hypothesized that the increased survival with scaffold implantation may reflect a differential distribution of CD11b⁺Gr-1^{hi}Ly6C⁻ cells at the primary tumor (local) and the spleen (systemic). Flow cytometric analysis indicated that the abundance of CD11b⁺Gr-1^{hi}Ly6C⁻ cells was reduced in mice receiving a scaffold implant versus mice receiving a mock surgery examined at day 10 after tumor inoculation. The burden of CD11b⁺Gr-1^{hi}Ly6C⁻ cells was reduced by 39% in the primary tumor (Fig. 7A) and 30% in the spleen (Fig. 7B, $N \geq 7$, $P < 0.05$ as determined by t-test in both cases). This result suggests that, in part, the presence of the scaffold contributes to a reduction in the abundance of key niche cells locally (i.e., primary tumor site) and systemically (i.e., spleen) that support metastasis. This observation was further investigated via Gr-1 antibody depletion of CD11b⁺Gr-1^{hi}Ly6C⁻ cells *in vivo*, which was performed in the

context of surgical resection (Supplementary Fig. S6). Mice receiving a mock surgery with Gr-1 depletion demonstrated survival greater than 20% by day 40 (Fig. 7C), with no survival observed at this time without Gr-1 depletion (Fig. 6C). Furthermore, with Gr-1 depletion, the observed difference in survival between mock and scaffold groups was not statistically significant (Fig. 7C), further supporting the involvement of CD11b⁺Gr-1^{hi}Ly6C⁻ cells in improving disease-specific survival in our model. Taken together, these results highlight the potential for PCL scaffold in improving disease-specific survival outcomes.

Discussion

In this study, microporous PCL scaffolds, implanted prior to tumor initiation, recruited metastatic cells at an early time point in disease progression. The novel approach to this work was based on recapitulating some of the immunological aspects of the pre-metastatic niche, while prior reports have focused on materials to mimic properties of target organs (e.g., bone, refs. 33, 34; bone marrow, ref. 35). Previous elegant studies of the pre-metastatic niche have identified some of the biological cues involved in cancer cell recruitment, such as the cellular components (e.g., hematopoietic and endothelial progenitor cells, immune cells), soluble factors (e.g., cytokines, chemokines), and ECM proteins (12, 14–17). Importantly, as indicated by Lyden (12, 18), the existence of the pre-metastatic niche implies that metastasis to a particular site is not random, but is predetermined, which supports the idea that a site could be engineered to attract metastatic cells. A synthetic scaffold provides an opportunity to create a defined environment to investigate the role of specific components involved in the colonization of metastatic cells. Scaffolds can be modified with specific niche components, such as stromal cells, ECM molecules, and cytokines to identify the key signals in the metastatic environment (36, 37), thereby providing a tool
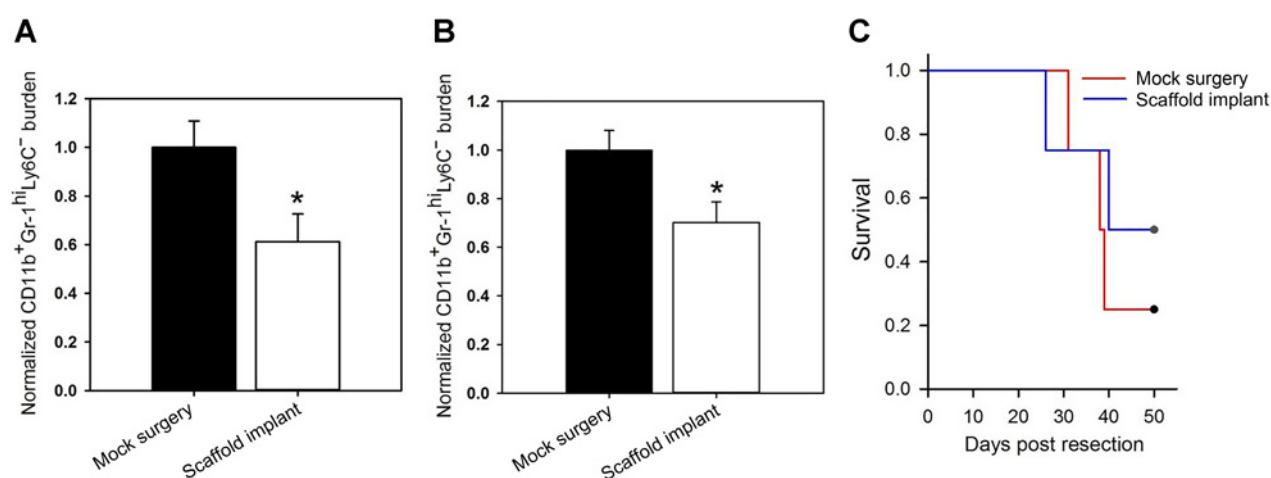
Figure 7.
Microporous PCL scaffolds reduce burden of CD11b$^+$Gr-1^{hi}Ly6C$^-$ cells in the primary tumor (**A**) and the spleen (**B**) in BALB/c mice. The percentage of CD11b$^+$ Gr-1^{hi} Ly6C$^-$ cells in the CD45$^+$ leukocyte population was examined at day 10 after tumor inoculation via flow cytometry and is reported as normalized burden ($N = 7$ for mock surgery; $N = 8$ for scaffold implant; *, $P < 0.05$ as determined using t test). **C,** anti-Gr-1 depletion of CD11b$^+$Gr-1^{hi}Ly6C$^-$ cells enhances survival in both mock and scaffold groups and diminishes the survival advantage observed for PCL implanted mice ($N = 4$ per group). Error bars, SEM.

with which to advance fundamental studies of the pre-metastatic niche and tumor metastasis. Herein, the scaffold defines a site for immune cell infiltration, and we characterize the dynamic immune response associated with cancer cell recruitment.

The immune cell populations at the PCL scaffold, which had stabilized prior to tumor inoculation, were substantially altered after tumor inoculation, suggesting that the changing foreign body response to the implant may contribute to metastatic cell recruitment. Immune cells are recognized as significant to the pre-metastatic niche (15, 25–30). As such, chemokine CCL-2 recruits inflammatory monocytes (Ly6C$^+$F4/80$^-$ cells) to the pre-metastatic niche enabling metastasis of breast cancer cells (28). Similarly, CD11b$^+$Gr-1^{hi}Ly6C$^-$ cells are recruited via inflammatory chemoattractants (e.g., S100A8 and S100A9) to pre-metastatic niches (38). In addition, CD11b$^+$Gr-1^{hi}Ly6C$^-$ cells are known to downregulate infiltration and suppress the function of T cells (CD4$^+$ and CD8$^+$ T cells) and NK cells (38–41). Consistent with these observations, we found an increase in the levels of monocytes and CD11b$^+$Gr-1^{hi}Ly6C$^-$ cells at the scaffold site after tumor inoculation and an associated decrease in the abundance of CD4$^+$ T cells, CD8$^+$ T cells, and CD49b$^+$ NK cells, with the greatest change observed for CD11b$^+$Gr-1^{hi}Ly6C$^-$ cells (i.e., more than 2 orders of magnitude). Importantly, the changing immune composition as a consequence of disease progression observed in the spleen largely reflected the dynamics at the scaffold site. Taken together, these results suggest that engineering a local microenvironment may be used to identify and modulate key components of cancer-associated immunogenicity in the pre-metastatic niche.

The implantation of PCL scaffolds enhanced disease-specific survival, which we hypothesized to be related to the decreased tumor burden in major organ sites and a reduction in systemic availability of key immune cells that support metastasis. The implantation of PCL scaffolds in the subcutaneous space reduced tumor burden in major organ sites (i.e., liver and brain) in an immunocompetent mouse model. We previously reported a reduction in burden in the lung in an immunocompromised mouse model using PLG scaffolds implanted in the intraperitoneal fat pad after tumor inoculation (11). The results

of the current study extend our previous observation and importantly suggest that a scaffold-based approach can contribute to the reduction in disease burden in solid organs in both immunocompetent and compromised mouse models and when implanted at different sites. Metastatic cells could be detected within chronically implanted PCL scaffolds by day 5 following tumor inoculation using ISOCT imaging, which allowed for label-free detection of metastasis through changes in the tissue ultrastructure (e.g., matrix organization) and the presence of cancer cells that have a distinct nanoscale signature relative to normal cells (22). In order to use ISOCT analysis for diagnostic screening of early metastasis, ultrastructural parameters measured with ISOCT (D, correlation length Ln, and refractive index fluctuation Bn), which independently change in the presence of carcinogenic tissue modification, would need to be investigated to establish a multivariate diagnostic for patients with metastatic disease.

The resection of the primary tumor at day 10 after tumor inoculation resulted in increased survival in mice that received a scaffold. The increased survival may result from a decreased burden of CD11b$^+$Gr-1^{hi}Ly6C$^-$ cells observed locally at the primary tumor and systemically in the spleen of a scaffold-bearing mouse when compared with a mouse that received a mock surgery. Gr-1 depletion studies further supported this observation, as mice receiving a mock surgery survive longer in the context of Gr-1 depletion, and the difference between mock and scaffold groups was abrogated with Gr-1 depletion. As stated, CD11b$^+$Gr-1^{hi}Ly6C$^-$ cells or myeloid derived suppressor cells (MDSC) have been implicated in the pre-metastatic niche and the reduced abundance of these cells systemically may contribute to the reduced burden in solid organs and, ultimately, to enhanced survival (42–44). Finally, MDSCs have been identified in high numbers in patients with metastatic disease, correlating with clinical stage and metastatic disease burden, and their levels are predictive of overall survival (45–47). Thus, a scaffold-based approach that reduces the abundance of MDSCs could, in part, explain the survival benefit observed in our studies. Taken together, the ability to detect metastatic disease at an early stage, in

combination with the survival benefit provided by the scaffold, highlights the potential for this technology in transforming the current detection and management of metastatic disease.

The recruitment of metastatic cells to the scaffold, combined with label-free imaging for detection of nascent stage metastatic cells, and reduced burden of disease in solid organs (i.e., liver and brain), may ultimately allow for interventions when the disease burden is low that could translate to improved disease-specific outcomes. In the clinical setting, the scaffold may be integrated into disease management plans by potentially serving as a sentinel site for detection of disease metastasis or recurrence. For example, the scaffold could be implanted in patients with a diagnosis of invasive cancer at the completion of adjuvant therapy, and monitored during scheduled follow-up visits using the optical imaging technique. If metastatic or recurrent disease was then detected, the scaffold could be explanted for cell retrieval and analysis to help guide targeted treatment decisions. Furthermore, in the setting of metastatic disease, given the potential survival benefit of the presence of the scaffold, patients may have extended disease-specific survival with excision of the primary tumor and scaffold implantation long term. Finally, the scaffold may be implanted prophylactically to help detect early onset metastatic disease in high-risk patients.

Our results provide the first evidence that a scaffold for capture and detection of early metastatic cells, combined with an intervention shortly after detection of early metastasis (i.e., primary tumor excision), can enhance survival. This biomaterial approach is based on the host response to an implanted scaffold, thereby avoiding the presence of potentially deleterious cellular or biological components. PCL material is currently FDA approved for applications such as drug delivery, suture material, and wound dressings, which may facilitate translation to the clinic for the capture of metastatic cells (48). Also, this material is biodegradable and would not need to be retrieved unless cancer cells are detected; and the degradation rate is relatively slow allowing the implant to be monitored for up to 2 years within a patient (49, 50). Clinical studies would be necessary to appropriately integrate metastatic cell-capturing scaffolds into existing breast cancer management plans. Taken together, the results of this work showing prolonged survival with scaffold implantation hold promise for reducing breast cancer morbidity and mortality.

References

1. Gupta GP, Massague J. Cancer metastasis: building a framework. Cell 2006;127:679–95.
2. Chaffer CL, Weinberg RA. A perspective on cancer cell metastasis. Science 2011;331:1559–64.
3. Chambers AF, Groom AC, MacDonald IC. Dissemination and growth of cancer cells in metastatic sites. Nat Rev Cancer 2002;2:563–72.
4. Murakami R, Kumita S, Yoshida T, Ishihara K, Kiriyama T, Hakozaki K, et al. FDG-PET/CT in the diagnosis of recurrent breast cancer. Acta Radiol 2012;53:12–6.
5. Engelhard K, Hollenbach HP, Wohlfart K, von Imhoff E, Fellner FA. Comparison of whole-body MRI with automatic moving table technique and bone scintigraphy for screening for bone metastases in patients with breast cancer. Eur Radiol 2004;14:99–105.
6. Lauenstein TC, Goehde SC, Herborn CU, Goyen M, Oberhoff C, Debatin JF, et al. Whole-body MR imaging: evaluation of patients for metastases. Radiology 2004;233:139–48.
7. Maheswaran S, Haber DA. Circulating tumor cells: a window into cancer biology and metastasis. Curr Opin Genet Dev 2010;20:96–9.
8. Yu M, Stott S, Toner M, Maheswaran S, Haber DA. Circulating tumor cells: approaches to isolation and characterization. J Cell Biol 2011;192:373–82.
9. Joosse SA, Pantel K. Biologic challenges in the detection of circulating tumor cells. Cancer Res 2013;73:8–11.
10. Paterlini-Brechot P, Benali NL. Circulating tumor cells (CTC) detection: clinical impact and future directions. Cancer Lett 2007;253:180–204.
11. Azarin SM, Yi J, Gower RM, Aguado BA, Sullivan ME, Goodman AG, et al. In vivo capture and label-free detection of early metastatic cells. Nat Commun 2015;6:8094.
12. Kaplan RN, Riba RD, Zacharoulis S, Bramley AH, Vincent L, Costa C, et al. VEGFR1-positive haematopoietic bone marrow progenitors initiate the pre-metastatic niche. Nature 2005;438:820–7.
13. Kaplan RN, Rafii S, Lyden D. Preparing the "soil": the premetastatic niche. Cancer Res 2006;66:11089–93.
14. Psaila B, Lyden D. The metastatic niche: adapting the foreign soil. Nat Rev Cancer 2009;9:285–93.

15. Peinado H, Lavotshkin S, Lyden D. The secreted factors responsible for pre-metastatic niche formation: old sayings and new thoughts. Semin Cancer Biol 2011;21:139–46.

16. Paget S. The distribution of secondary growths in cancer of the breast. Lancet 1889;133:571–3.

17. Fidler IJ. The pathogenesis of cancer metastasis: the `seed and soil' hypothesis revisited. Nat Rev Cancer 2003;3:453–8.

18. Kaplan RN, Psaila B, Lyden D. Bone marrow cells in the pre-metastatic niche': within bone and beyond. Cancer Metastasis Rev 2006;25:521–9.

19. Jang JH, Rives CB, Shea LD. Plasmid delivery in vivo from porous tissue-engineering scaffolds: transgene expression and cellular transfection. Mol Ther 2005;12:475–83.

20. Yi J, Backman V. Imaging a full set of optical scattering properties of biological tissue by inverse spectroscopic optical coherence tomography. Opt Lett 2012;37:4443–5.

21. Yi J, Radosevich AJ, Rogers JD, Norris SCP, Capoglu IR, Taflove A, et al. Can OCT be sensitive to nanoscale structural alterations in biological tissue? Opt Express 2013;21:9043–59.

22. Yi J, Radosevich AJ, Stypula-Cyrus Y, Mutyal NN, Azarin SM, Horcher E, et al. Spatially resolved optical and ultrastructural properties of colorectal and pancreatic field carcinogenesis observed by inverse spectroscopic optical coherence tomography. J Biomed Opt 2014;19:36013.

23. Milsom CC, Lee CR, Hackl C, Man S, Kerbel RS. Differential post-surgical metastasis and survival in SCID, NOD-SCID and NOD-SCID-IL-2Rgamma (null) mice with parental and subline variants of human breast cancer: implications for host defense mechanisms regulating metastasis. PLoS One 2013;8:e71270.

24. Guerin E, Man S, Xu P, Kerbel RS. A model of postsurgical advanced metastatic breast cancer more accurately replicates the clinical efficacy of antiangiogenic drugs. Cancer Res 2013;73:2743–8.

25. Kitamura T, Qian BZ, Pollard JW. Immune cell promotion of metastasis. Nat Rev Immunol 2015;15:73–86.

26. Hiratsuka S, Watanabe A, Aburatani H, Maru Y. Tumour-mediated upregulation of chemoattractants and recruitment of myeloid cells predetermines lung metastasis. Nat Cell Biol 2006;8:1369–75.

27. Sceneay J, Chow MT, Chen A, Halse HM, Wong CS, Andrews DM, et al. Primary tumor hypoxia recruits CD11b+/Ly6Cmed/Ly6G+ immune suppressor cells and compromises NK cell cytotoxicity in the premetastatic niche. Cancer Res 2012;72:3906–11.

28. Qian BZ, Li J, Zhang H, Kitamura T, Zhang J, Campion LR, et al. CCL2 recruits inflammatory monocytes to facilitate breast-tumour metastasis. Nature 2011;475:222–5.

29. Erler JT, Bennewith KL, Cox TR, Lang G, Bird D, Koong A, et al. Hypoxia-induced lysyl oxidase is a critical mediator of bone marrow cell recruitment to form the premetastatic niche. Cancer Cell 2009;15:35–44.

30. Qian B, Deng Y, Im JH, Muschel RJ, Zou Y, Li J, et al. A distinct macrophage population mediates metastatic breast cancer cell extravasation, establishment and growth. PLoS One 2009;4:e6562.

31. Radosevich AJ, Mutyal NN, Yi J, Stypula-Cyrus Y, Rogers JD, Goldberg MJ, et al. Ultrastructural alterations in field carcinogenesis measured by enhanced backscattering spectroscopy. J Biomed Opt 2013;18:097002.

32. Radosevich AJ, Mutyal NN, Rogers JD, Gould B, Hensing TA, Ray D, et al. Buccal spectral markers for lung cancer risk stratification. PLoS One 2014;9:e110157.

33. Moreau JE, Anderson K, Mauney JR, Nguyen T, Kaplan DL, Rosenblatt M. Tissue-engineered bone serves as a target for metastasis of human breast cancer in a mouse model. Cancer Res 2007;67:10304–8.

34. Holzapfel BM, Wagner F, Loessner D, Holzapfel NP, Thibaudeau L, Crawford R, et al. Species-specific homing mechanisms of human

35. prostate cancer metastasis in tissue engineered bone. Biomaterials 2014;35:4108–15.

35. Seib FP, Berry JE, Shiozawa Y, Taichman RS, Kaplan DL. Tissue engineering a surrogate niche for metastatic cancer cells. Biomaterials 2015;51:313–9.

36. Lee J, Li M, Milwid J, Dunham J, Vinegoni C, Gorbatov R, et al. Implantable microenvironments to attract hematopoietic stem/cancer cells. Proc Natl Acad Sci U S A 2012;109:19638–43.

37. Bersani F, Lee J, Yu M, Morris R, Desai R, Ramaswamy S, et al. Bioengineered implantable scaffolds as a tool to study stromal-derived factors in metastatic cancer models. Cancer Res 2014;74:7229–38.

38. Markowitz J, Wesolowski R, Papenfuss T, Brooks TR, Carson WE3rd. Myeloid-derived suppressor cells in breast cancer. Breast Cancer Res Treat 2013;140:13–21.

39. Hanson EM, Clements VK, Sinha P, Ilkovitch D, Ostrand-Rosenberg S. Myeloid-derived suppressor cells down-regulate L-selectin expression on CD4+ and CD8+ T cells. J Immunol 2009;183:937–44.

40. Elkabets M, Ribeiro VS, Dinarello CA, Ostrand-Rosenberg S, Di Santo JP, Apte RN, et al. IL-1beta regulates a novel myeloid-derived suppressor cell subset that impairs NK cell development and function. Eur J Immunol 2010;40:3347–57.

41. Hoechst B, Voigtlaender T, Ormandy L, Gamrekelashvili J, Zhao F, Wedemeyer H, et al. Myeloid derived suppressor cells inhibit natural killer cells in patients with hepatocellular carcinoma via the NKp30 receptor. Hepatology 2009;50:799–807.

42. Srivastava MK, Zhu L, Harris-White M, Kar U, Huang M, Johnson MF, et al. Myeloid suppressor cell depletion augments antitumor activity in lung cancer. PLoS One 2012;7:e40677.

43. Li Z, Pang Y, Gara SK, Achyut B, Heger C, Goldsmith PK, et al. Gr1+ CD11b+ cells are responsible for tumor promoting effect of TGFβ in breast cancer progression. Int J Cancer 2012;131:2584–95.

44. Kohanbash G, McKaveney K, Sakaki M, Ueda R, Mintz AH, Amankulor N, et al. GM-CSF promotes the immunosuppressive activity of glioma-infiltrating myeloid cells through interleukin-4 receptor-α;. Cancer Res 2013;73:6413–23.

45. Diaz-Montero CM, Salem ML, Nishimura MI, Garrett-Mayer E, Cole DJ, Montero AJ. Increased circulating myeloid-derived suppressor cells correlate with clinical cancer stage, metastatic tumor burden, and doxorubicin-cyclophosphamide chemotherapy. Cancer Immunol Immunother 2009;58:49–59.

46. Almand B, Resser JR, Lindman B, Nadaf S, Clark JI, Kwon ED, et al. Clinical significance of defective dendritic cell differentiation in cancer. Clin Cancer Res 2000;6:1755–66.

47. Cole S, Montero A, Garret-Mayer E, Onicescu G, Vandenberg T, Hutchens S, et al. Elevated Circulating Myeloid Derived Suppressor Cells (MDSC) Are Associated with Inferior Overall Survival (OS) and Correlate with Circulating Tumor Cells (CTC) in Patients with Metastatic Breast Cancer. In: Thirty-Second Annual CTRCAACR San Antonio Breast Cancer Symposium: Cancer Research, San Antonio, TX2009.

48. Couet F, Rajan N, Mantovani D. Macromolecular biomaterials for scaffold-based vascular tissue engineering. Macromol Biosci 2007;7:701–18.

49. Sung HJ, Meredith C, Johnson C, Galis ZS. The effect of scaffold degradation rate on three-dimensional cell growth and angiogenesis. Biomaterials 2004;25:5735–42.

50. Kohn J, Abramson S, Langer R. Bioresorbable and Bioerodible Materials, In: Ratner BD, Hoffman AS, Schoen FJ, andLemons JE, editors. Biomaterials Science: An Introduction to Materials in Medicine. San Diego: Elsevier Academic Press; 2004. p.115–27.

AAGR American Association for Cancer Research

Enhanced Survival with Implantable Scaffolds That Capture Metastatic Breast Cancer Cells *In Vivo*

Shreyas S. Rao, Grace G. Bushnell, Samira M. Azarin, et al.

Updated version	Access the most recent version of this article at: http://cancerres.aacrjournals.org/content/76/18/5209
Supplementary Material	Access the most recent supplemental material at: http://cancerres.aacrjournals.org/content/suppl/2016/09/21/76.18.5209.DC1

Cited articles	This article cites 48 articles, 12 of which you can access for free at: http://cancerres.aacrjournals.org/content/76/18/5209.full#ref-list-1

E-mail alerts	Sign up to receive free email-alerts related to this article or journal.
Reprints and Subscriptions	To order reprints of this article or to subscribe to the journal, contact the AACR Publications Department at pubs@aacr.org.
Permissions	To request permission to re-use all or part of this article, use this link http://cancerres.aacrjournals.org/content/76/18/5209. Click on "Request Permissions" which will take you to the Copyright Clearance Center's (CCC) Rightslink site.